THE JOURNAL OF BIOLOGICAL CHEMISTRY VOL. 289, NO. 3, pp. 1742–1755, January 17, 2014

Structural Basis for Autoinhibition of CTP:Phosphocholine Cytidylyltransferase (CCT), the Regulatory Enzyme in Phosphatidylcholine Synthesis, by Its Membrane-binding Amphipathic Helix*

Received for publication, October 16, 2013, and in revised form, November 18, 2013 Published, JBC Papers in Press, November 25, 2013, DOI 10.1074/jbc.M113.526970

Jaeyong Lee[‡], **Svetla G. Taneva**[‡], **Bryan W. Holland**[§], **D. Peter Tieleman**[§1], **and Rosemary B. Cornell**[‡¶2]

From the Departments of [‡]*Molecular Biology and Biochemistry and* [¶]*Chemistry, Simon Fraser University, Burnaby, British Columbia V5A 1S6, Canada and* [§]*Department of Biological Sciences, University of Calgary, Calgary, AlbertaT2N 1N4, Canada*

Background: The CCT M-domain contains an autoinhibitory (AI) segment, but its mechanism was obscure.
Results: The AI helix partly occludes active site access and engages a mobile loop (L2), impeding the dynamics of key catalytic lysine 122.
Conclusion: Loop L2 is a key target of the AI clamp.
Significance: This work reveals the nature of a regulatory off-switch in an enzyme regulated by membrane binding.

CTP:phosphocholine cytidylyltransferase (CCT) interconverts between an inactive soluble and active membrane-bound form in response to changes in membrane lipid composition. Activation involves disruption of an inhibitory interaction between the αE helices at the base of the active site and an autoinhibitory (AI) segment in the regulatory M domain and membrane insertion of the M domain as an amphipathic helix. We show that in the CCT soluble form the AI segment functions to suppress k_{cat} and elevate the K_m for CTP. The crystal structure of a CCT dimer composed of the catalytic and AI segments reveals an AI-αE interaction as a cluster of four amphipathic helices (two αE and two AI helices) at the base of the active sites. This interaction corroborates mutagenesis implicating multiple hydrophobic residues within the AI segment that contribute to its silencing function. The AI-αE interaction directs the turn at the C-terminal end of the AI helix into backbone-to-backbone contact with a loop (L2) at the opening to the active site, which houses the key catalytic residue, lysine 122. Molecular dynamics simulations suggest that lysine 122 side-chain orientations are constrained by contacts with the AI helix-turn, which could obstruct its engagement with substrates. This work deciphers how the CCT regulatory amphipathic helix functions as a silencing device.

Amphitropic enzymes are a class of enzymes whose regulatory ligand takes the form of a membrane. How membrane binding activates catalytic function in these proteins is generally not well understood, although recent progress has been made for several lipid-activated kinases (1). CCT[3] is a prototypical amphitropic enzyme whose function is to control membrane phosphatidylcholine (PC) homeostasis (2). It catalyzes the rate-limiting step in PC synthesis, the formation of the headgroup donor, CDP-choline. In addition to its role in maintaining membrane phospholipid compositional balance, targeted gene deletions or siRNA-mediated suppression have revealed the involvement of the major isoform, CCTα, in lung surfactant production (3), plasma lipoprotein balance (4), size regulation of lipid storage droplets (5), and control of diacylglycerol concentration in the Golgi, which in turn regulates vesicular traffic (6).

CCTs from yeast to humans contain a catalytic α/β fold (7) followed by a membrane binding region and a disordered C-terminal tail. The α/β fold catalyzes a nucleophilic attack of phosphocholine on the α-phosphate of CTP to generate CDP-choline and diphosphate. The reaction proceeds via a random order sequential mechanism (8). Catalysis is accomplished by surrounding the α-phosphates of CTP and phosphocholine with amine-containing groups supplied by several loops forming the active site that provide charge stabilization and adapt the geometry about the α-phosphate of CTP (7). Extensive mutagenesis of active site residues has highlighted the key importance of lysine 122 (Lys^{122}) in loop L2. Replacement with other residues (even conservative arginine), cripples k_{cat}/K_m by 5 orders of magnitude (9).[4]

The membrane binding domain contains an inducible amphipathic helix (domain M) that detects physical properties of a PC-deficient membrane, such as high negative charge density and lipid packing stress (11–14). An encounter with such a

* This work was supported in part by Canadian Institutes of Health Research Grants MT-12134 (to R. B. C.) and MOP-62690 (to D. P. T.).
The atomic coordinates and structure factors (codes 4MVD and 4MVC) have been deposited in the Protein Data Bank (http://wwpdb.org/).
[1] An Alberta Innovates Health Solutions Scientist and Alberta Innovates Technology Futures Strategic Chair in (Bio) Molecular Simulation.
[2] To whom correspondence should be addressed: Dept. of Molecular Biology and Biochemistry, Simon Fraser University, Burnaby, British Columbia V5A 1S6, Canada. Tel.: 778-782-3709; Fax: 778-782-5583; E-mail: cornell@sfu.ca.

[3] The abbreviations used are: CCT, CTP:phosphocholine cytidylyltransferase; AI, autoinhibitory; PC, phosphatidylcholine; PG, phosphatidylglycerol; AMBER, Assisted Model Building and Energy Refinement; CCP4, Collaborative Computational Project 4; GROMACS, Groningen Machine for Chemical Simulations; VMD, Visual Molecular Dynamics; MD, molecular dynamics; r.m.s.d., root mean square deviation.
[4] We use the following definition of k_{cat}/K_m: the rate constant associated with the formation of a productive ES complex that will proceed to product (10).

membrane surface triggers insertion of the hydrophobic face of the amphipathic helix (15) and transduces a conformational change in the catalytic domain associated with an increase in k_{cat}/K_m of nearly 3 orders of magnitude (16–18). This process restores the membrane PC content. When not membrane-engaged, this same M domain functions as an autoinhibitory device. Deletion or mutagenesis of domain M results in a ~20-fold increment in constitutive (lipid-independent) activity with a 10-fold increase in the maximum velocity and a ~2-fold decrease in the Michaelis constant (K_m) for CTP (16–18). The K_m for the other substrate, phosphocholine, is not regulated. However, membrane binding, which requires a functioning M domain, imparts an additional order of magnitude increase in catalytic efficiency above the increase observed upon domain M deletion (16). These data suggest that M has a dual role in CCT regulation: as a silencer in the soluble form and as an activator in its membrane-bound form. In this work, we have focused on the autoinhibitory role of M in the silenced, soluble form of CCT.

How does domain M impart catalytic silencing? Previous data suggest that most of domain M has a high degree of disorder in the CCT soluble form. Circular dichroism analyses revealed that the α-helical content increases by nearly 60 residues upon membrane binding mostly at the expense of disordered conformers (19). Protease accessibility, photocross-linking, and site-directed fluorescence anisotropy suggested a bipartite structure for domain M in the CCT soluble form: an N-terminal disordered segment (residues ~235–270) followed by a more structured segment (residues 272–301) (20, 21). This bipartite structure is also predicted by many disorder prediction algorithms and is a feature of CCT M domains across phyla (16, 22).

A recent analysis of chimeric enzymes revealed that the regulation of the catalytic domain of rat CCTα is tolerant of large variation in the sequence and length of the M domain, suggesting that physical features, such as hydrophobicity and amphipathy, are more important than sequence (16). However, deletion of a relatively conserved 22-mer from the C-terminal end generated a deregulated enzyme with catalytic properties similar to that of CCT-236, which is missing the entire M domain (16). We refer to this 22-mer segment as the AI motif (see Fig. 1*A*). Denaturation analysis of this segment in the CCT soluble form suggested a weakly folded conformation in contrast to an absence of structure in the rest of domain M (21).

Does the AI motif interact with the catalytic domain and, if so, where? Cysteine engineering of scattered sites within domain M followed by photocross-linking and mass spectrometry identified an association with the helix αE pair extending from the base of the active site of the catalytic dimer. This interaction was confirmed by deuterium exchange/mass spectrometry (21). Contacts were broken in the presence of activating lipid vesicles, suggesting a silencing function. Activation of CCT, according to the emerging model, involves the dissociation of the AI motif from αE and its association with the membrane surface. Essentially there is a competition between the αE helices and the membrane for an emergent AI helix. The flexible leash portion of domain M would serve to facilitate the transitions of the AI helix. Although this work identified three components of the CCT autoinhibitory interaction, the AI motif, the leash, and the helix αE docking site, the chemical nature of the docking interaction and the mechanism of silencing were not explained.

Here we present mutagenesis analysis of the AI segment to further define its role as a suppressor of catalysis in the CCT soluble form. We solved the crystal structure of a mammalian CCT containing both the catalytic and M domains, revealing the nature of the AI-αE interaction and a plausible mechanism for catalytic silencing. Molecular dynamics simulations support that mechanism, which involves a clamp on an active site loop and restriction of the orientation of the key catalytic residue, Lys^{122}.

EXPERIMENTAL PROCEDURES

Preparation of CCT Constructs

All CCTs were derived from rat CCTα (UniProtKB/Swiss-Prot accession number P19836). The sequence fidelity of all CCT constructs was confirmed by two-strand sequencing.

CCT-367—The preparation of wild-type, full-length CCT-367 plasmid and its expression and purification were described in Taneva *et al.* (19).

pET14b-CCT Constructs—The preparation of pET14b CCT-236(K122A) was described in Taneva *et al.* (23). The wild-type residue, Lys^{122}, was restored by swapping a KpnI/SacI 650-bp fragment from pET14b-CCT-312. We prepared pET14b CCT-312 as follows. Using pAX142-HisCCTα-312 (22) as the template, the opening reading frame encoding CCT(1–312) was PCR-amplified with 5′-ATAT*CATATG*GATGCACAGAGTTCAG-3′ and 5′-ATAT*GGATCC*TCACTGCAGCATCCGA-3′ oligonucleotide primers containing NdeI and BamHI restriction sites, respectively (sites in italics). The PCR fragment was double digested using NdeI/BamHI and cloned into similarly digested pET14b plasmid. We prepared the leash deletion variants, pET14b CCT-312(Δ252–269) and pET14b CCT-312(Δ238–269), which we refer to as CCT-312(Δ18) and CCT-312(Δ32), respectively, by QuikChange mutagenesis (Stratagene) using pET14b CCT-312 with the wild-type sequence as a template and primers that spanned the codons to be deleted. The forward primers were 5′-GA GTT GAT AAG GTA AAG AAG . . . AAG AGC ATC GAC CTC AT-3′ for CCT-312(Δ18) and 5′-AT GTC AGC TTT ATC AAC GAA . . . AAG AGC ATC GAC CTC ATC-3′ for CCT-312(Δ32). The gap indicates the site of deletion. The domain M truncations at codon 304, 293, 271, or 255 were generated by QuikChange mutagenesis using primers that engineered a stop codon after the terminal codon to be expressed. The template for these variants was pET14b HisCCT-312 with the wild-type sequence. All CCT constructs in pET14b had a plasmid-derived sequence ($MGSSH_6$SSGLVPRGSH) N-terminal to the CCT Met-1.

pAX142-CCT Full-length Constructs—The series of domain M variants with serine or alanine substitutions at 6, 8, or 10 hydrophobic residues in the AI motif were created in the COS cell expression vector pAX142. The pAX142 template used for mutagenesis contained a full-length CCT-367 with a single cysteine at residue 288 (21). This version was used to incorporate a fluorophore at one site in that work and has near-WT activity (21). This construct also has an N-terminal His tag that adds the

sequence $MAKH_6IEGRSA$ before the first methionine of CCT. Using pAX142 HisCCT-367(S288C) as template, we created pAX142 versions of CCT-367(6S) and CCT-367(6A) by making serine or alanine substitutions at codons 285, 286, 289, 290, 292, and 293 using mutagenic primers and QuikChange mutagenesis. We made CCT-367(8S) using CCT-367(6S) as the template and engineering additional serine substitutions at residues 275 and 278. To make CCT-367(10S), we used the CCT-367(8S) template and another round of QuikChange to engineer additional serine mutations at residues 272 and 274.

Bacterial Expression and Purification of CCT-312, CCT-312(Δ18), and CCT-312(Δ32) for Crystallization

A single colony of Rosetta cells harboring the pET14b-CCT plasmid was grown in 1 liter of LB medium with 0.3 mM ampicillin and 0.1 mM chloramphenicol. After ~5 h at 37 °C, CCT expression was induced with 1 mM isopropyl 1-thio-β-D-galactopyranoside and incubation at 20 °C for 3 h. Cells were harvested by centrifugation at 4500 rpm for 15 min and stored at −80 °C. The frozen cell pellet (~1.7 g) was resuspended in 30 ml of lysis buffer (10 mM Tris, pH 8.0, 150 mM NaCl, 2 mM DTT, 0.2 mg/ml lysozyme, 1% Triton X-100, and 25 units of the nuclease Benzonase). After incubation for 30 min at 4 °C, lysis was completed by probe sonication with three maximum pulses for 30 s on ice. The crude cell lysate was centrifuged at 23,300 × *g* for 30 min. The supernatant fraction (30 ml) was loaded onto 4 ml of nickel-agarose beads in a column equilibrated with EQ buffer (10 mM Tris, pH 8.0, 150 mM NaCl, 2 mM DTT, and 25 mM imidazole). The beads were washed with 10 ml of EQ buffer with 0.5 M NaCl and then with 10 ml of EQ buffer. The bound His-CCT was eluted with 10 ml of EQ buffer containing 100 mM imidazole followed by 4 × 10-ml volumes of EQ buffer with 350 mM imidazole. Elution fractions with the highest CCT purity (assessed by gels) were pooled and further purified by ion exchange chromatography. HisCCT-312 was purified by SP-Sepharose, and HisCCT-312(Δ32) was purified by Q-Sepharose. Columns (4 ml) were washed with 10 ml of EQ buffer followed by 8 ml each of 200, 300, 400, and 500 mM NaCl in 10 mM Tris, pH 8.0 and 2 mM DTT. The fractions containing purified proteins were combined, concentrated, and buffer-exchanged with 10 mM Tris, pH 8.0, 300 mM NaCl, and 2 mM DTT using a 15-ml centrifugal filter device with 30-kDa cutoff (Millipore).

Bacterial Expression and Purification of CCT Truncation Variants

CCT-255, CCT-271, and CCT-293 were expressed in Rosetta cells as described (23) with minor modifications. The proteins were purified from the 20,000 × *g* supernatant using nickel-agarose at 4 °C (23). The peak elution fractions were dialyzed against 10 mM Tris, pH 7.4, 0.1 M NaCl, 0.15 mM Triton X-100, and 2 mM DTT and were frozen at −80 °C. CCT-304 was insoluble and was isolated from the 20,000 × *g* pellet fraction after urea denaturation, binding to nickel-agarose, on-resin refolding, and elution with imidazole (21). Peak fractions from the nickel-agarose column were dialyzed against the above buffer prior to storage.

Expression and Purification of Full-length His-tagged CCTs from the COS Cell System

CCT cDNAs incorporated into pAX142 plasmids were expressed in COS-1 cells using 48-h transfection (14). Cell pellets were lysed by sonication in 20 mM phosphate buffer, pH 7.4, 0.25 mM Triton X-100, 2 mM DTT, and a battery of protease inhibitors (24). NaCl was added to 0.5 M, and the lysates were sedimented at 20,000 × *g* for 10 min. HisCCT-367(8S) was purified from this supernatant using nickel-agarose (23). His-CCT-367(6A), -(6S), and -(10S) were mostly insoluble and were purified from the 20,000 × *g* pellet after washing the pellet by brief sonication in 10 mM Tris, pH 7.4, 0.5 M NaCl, 0.25 mM Triton X-100, protease inhibitors, and 2 mM DTT; collecting the insoluble material; and solubilizing it in 8 M urea. The urea-denatured HisCCT-367(6A) was purified and refolded using nickel-agarose chromatography (21). HisCCT-367(6S) and -(10S) were highly enriched in the supernatant after urea solubilization and were renatured slowly at 4 °C over ~24 h by sequential dialysis against a 300-fold volume excess of 10 mM Tris, pH 7.4, 0.1 M NaCl, 0.15 mM Triton X-100, and 2 mM DTT containing 5 M urea followed by 2.5 M urea and finally 0.5 M urea. The dialyzed sample was centrifuged 10 min at 20,000 × *g*, and the supernatant was saved for analysis. Although these concentrated protein preparations contained 0.5 M urea (to maintain solubility upon freeze-thaw), the urea concentration after dilution in the CCT activity assays was only ~4 mM. When assayed in the presence of saturating concentrations of PC/PG vesicles CCT-367(6S) and CCT-367(6A) had WT activity, suggesting complete refolding.

CCT Enzyme Activity Analysis

All CCT variants were analyzed using a standard assay (23, 25) in which substrate concentrations are optimal for WT CCT (16) in the absence or presence of egg PC/egg PG (1:1) sonicated vesicles (26). Lipid concentrations were 0.25–0.5 mM for maximal activation depending on the variant. Kinetic constants were obtained in separate trials where the CTP concentration was varied from 0 to 36 mM while maintaining the phosphocholine concentration at 2 mM. The velocity *versus* CTP concentration curves were evaluated using Prism 4 software and were fit to the Michaelis equation: $V = V_{max}[S]/(K_m + [S])$ where V_{max} is the velocity extrapolated to infinite [S] and K_m is the Michaelis constant. The constant k_{cat} was obtained by dividing the V_{max} by the molar concentration of the CCT.

Crystallization and Diffraction Data Collection of CCT-312 and CCT-312(Δ32)

Both protein crystals were grown by the vapor diffusion method at 22 °C in sitting drops composed of 1.5 μl of protein and 1.5 μl of the reservoir (1 ml). HisCCT-312 (~0.2 mM) with 2 mM CDP-choline crystallized in 0.1 M MES, pH 6.5, 1.80 M $(NH_4)_2SO_4$, and 3% dioxane. These rare crystals appeared within 1 week and matured over 4 weeks. CCT-312(Δ32) (~0.4 mM) with 4 mM CDP-choline crystallized in 0.1 M Tris, pH 8.5, 20% PEG 10,000, and 0.2 M sodium citrate. These crystals readily formed within a few days and matured over several weeks. The CCT-312 crystals were frozen in 0.1 M MES, pH 6.5, 1.80 M $(NH_4)_2SO_4$, 3% dioxane, and 20% glycerol. The CCT-312(Δ32)

crystals were frozen in 0.1 M Tris, pH 8.5, 20% PEG 10,000, 0.2 M sodium citrate, and 30% glycerol. The diffraction data sets for the CCT-312 and CCT-312(Δ32) crystals were collected at the Canadian Light Source using Beamline 08ID-1 and 08IB-1, respectively. The data sets were indexed and integrated using iMosflm 1.0.4 (27) and were subsequently merged using Scala (28) in the CCP4 Program Suite 6.1.3 (29).

Structure Determination and Refinement

Both structures were solved by molecular replacement using Phaser (30) in CCP4 6.1.3 (29). For the CCT-312 8.0-Å diffraction set, we initially used the CCT catalytic domain dimer excluding water (7) (Protein Data Bank code 3HL4) as the search model and found a molecular replacement solution that revealed the catalytic domain as well as additional tubular electron density adjacent to the αE helices. Subsequent model building and refinement resolved additional continuous and tubular electron densities that connected catalytic domains. These were modeled as extended polyalanine helices. The final model was tetrameric (dimer of dimers). After we had solved the 3-Å CCT-312(Δ32) dimer structure, we used it as a search model for the 8.0-Å data set instead of the CCT-236 structure. The structural outcomes of the molecular replacement and subsequent refinement were virtually the same. But there were significant statistical improvements. Both the log-likelihood-gain (LLG) score in Phaser and R_{work}/R_{free} values in REFMAC improved. The crystal structure had four dimers in the asymmetric unit, a very high calculated solvent content of 77.7%, and a Matthew's coefficient of 5.5 Å^3/Da (31). For CCT-312(Δ32), the molecular replacement solution placed one dimer in the asymmetric unit, and the structure had a calculated solvent content of 52.4% and a Matthew's coefficient of 2.6 Å^3/Da. For both structures, the membrane binding domain and AI motifs were built by several iterated cycles of manually fitting the corresponding electron density using the program Coot (32) followed by refinement using PHENIX (33) and REFMAC5 (34).

CD Analysis of the Secondary Structure of CCT-312 in Solution

CCT-312 (2 μM) in 0.22 μm-filtered 50 mM phosphate buffer, pH 7.4 was incubated for 2 min at 25 °C without or with lyso-PC/egg PG (4:1, mol/mol) micelles (19). CD spectra were recorded using a Jasco J-810 spectropolarimeter at 25 °C in a cell of 0.5-mm path length at a scanning rate of 100 nm/min and a bandwidth of 1 nm. Spectral resolution was 0.5 nm, and three scans were averaged per spectrum. All spectra were smoothed and corrected for the appropriate backgrounds (buffer or buffer + micelles) and were converted to units of molar ellipticity. Protein concentrations were determined by absorbance at 280 nm and calculated extinction coefficients. Secondary structure content was deconvoluted from the CD spectra by CDPro and protein reference set 7, which includes 43 soluble and five denatured proteins (35).

Molecular Dynamics Simulations

Simulations with and without CDP-choline were based on rat CCTα-236 (Protein Data Bank code 3HL4) (7) residues 40–236. CDP-choline was parametrized in a two-step process. We used Protein Data Bank code 3HL4 as a starting structure for density functional theory calculations through the "RESP ESP charge Derive Server" (R.E.D. Server) (36). The results were ported to the general AMBER force field (37) for the CDP-choline molecule for use with AMBER protein force fields. For testing the effects of bound AI motifs, the starting structure was the 3-Å CCT-312(Δ32) in this study. Two systems were created, one with and one without the bound AI helices. Neither of these contained bound CDP-choline. AI peptides were embedded in the starting structure as separate chains, and their termini were charged.

All simulations used version 4.6 of the GROMACS MD package (38) with the AMBER99SB-ildn atomistic force field (39) and the TIP3P (transferable intermolecular potential 3P) (transferable intermolecular potential 3P) model for water (40). All systems were hydrated to ~1.2 nm around the dimer using dodecahedron-shaped periodic boundary conditions. The systems were neutralized with an excess of Na^+, and the water was ionized to create a 0.15 M NaCl solution. The simulations were performed in an NPT ensemble with $T = 310$ K and $P = 1$ atm. The temperature was held constant using the stochastic "v-rescale" thermostat with a coupling parameter of 2.0 ps (41), and the pressure was maintained by isotropic "Parrinello-Rahman" coupling (42) with a τ_p of 5.5 ps and a compressibility of 4.5×10^{-5} bar^{-1}. Bonds were constrained using the LINCS algorithm (43) with a 2-fs time step. The van der Waals potential was cut off at 1.4 nm after being switched at 1.2 nm, and the electrostatic potential was also cut off at 1.4 nm to use the Verlet neighbor searching algorithm. Particle mesh Ewald (44) was used for long range electrostatics with a grid spacing of 0.1 nm. The CCT-236 simulations were equilibrated for 200 ps before analysis. The CCT-312(Δ32) systems were equilibrated for 10 ns to test the stability of the binding between the AI and αE helices. All systems were then evolved for a 200-ns production run, sampling every 5 ps. The finished trajectories were fitted (translated and rotated with solution removed) to the very stable β-sheets of both monomers. Trajectories were analyzed with VMD molecular visualization software (45) and GROMACS tools.

The structures reported here have been deposited with the Research Collaboratory for Structural Bioinformatics (RCSB) under Protein Data Bank codes 4MVC (CCT-312(Δ32) and 4MVD (CCT-312).

RESULTS

In the CCT Soluble Form (CCT_{sol}) the AI Segment Suppresses k_{cat}/K_m—We previously showed that deletion of the segment between residues 272 and 293 generated a desilenced CCT_{sol} with a maximal velocity nearly identical to that of the deletion of the entire regulatory tail (16). This result suggests a primary autoinhibitory role for the motif. However, one could argue that a large deletion within a domain could disrupt the structure and interactions of the whole domain. To further define the boundaries of the AI motif, we constructed a series of systematic truncations to test the role of the positively charged N-terminal portion of the M domain (CCT-255), the non-conserved midsection of domain M (CCT-271), and the AI motif (CCT-293 and CCT-304) (Fig. 1*A*). We determined the k_{cat} and CTP K_m values for these CCTs in the absence of lipids.

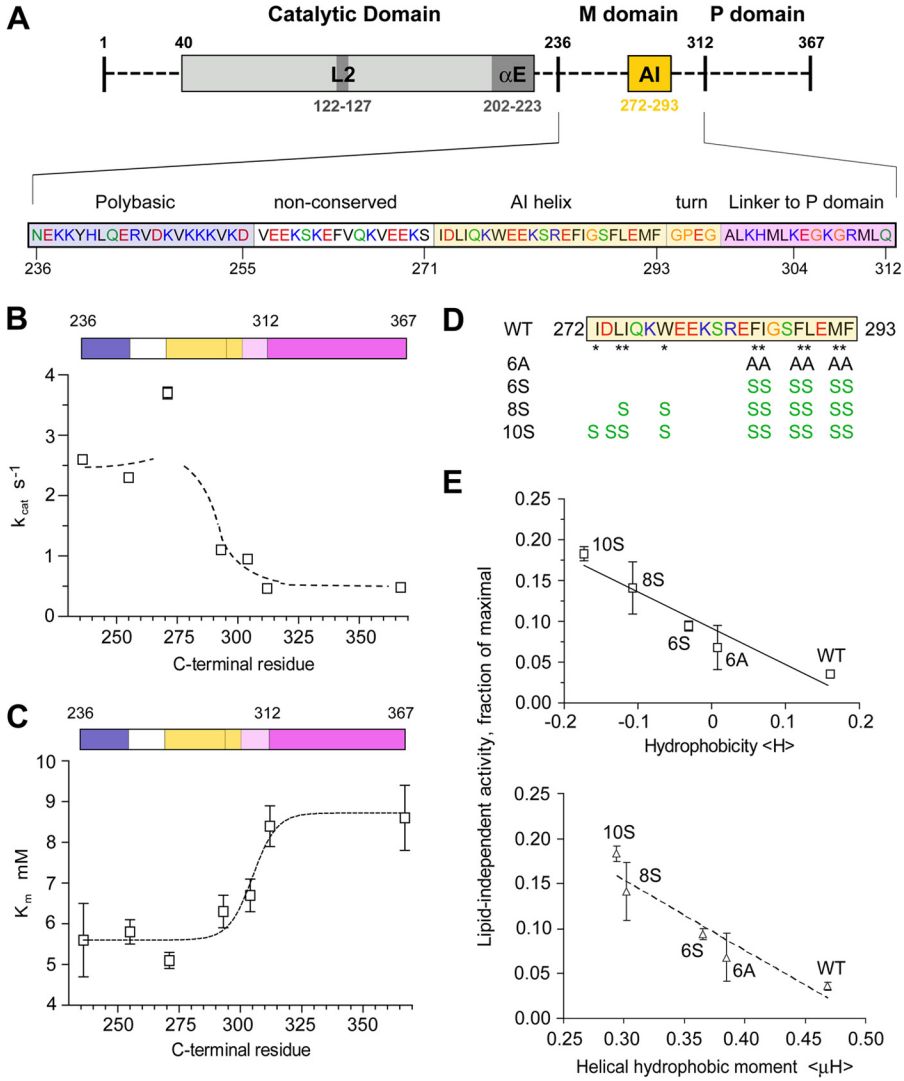

FIGURE 1. **The presence and amphipathy of the AI segment correlate with catalytic silencing.** *A*, domain structure of rat CCTα and the sequence of domain M and linker to region P showing the properties of the subregions. The *yellow shaded box* encompasses the autoinhibitory segment, which is a helix-turn in our solved structure. Amino acids are color-coded: *red*, acidic; *blue*, basic; *green*, polar; *black*, non-polar; *orange*, glycine and proline. *B* and *C*, effect of truncations on k_{cat} (*B*) and CTP K_m (*C*). The *colored bars* above the data represent the subregions of domain M/linker. Kinetic constants were determined in the absence of lipids using purified enzymes and variable CTP concentrations. The data are means ± 95% confidence interval. In *B*, the *error bars* are within the symbols. The *dashed lines* are guides only. *D*, hydrophobic residues (*asterisks*) in the AI motif were substituted with Ala or Ser for analysis of effects on CCT activity. *E*, silencing correlates with hydrophobicity and amphipathy of domain M. Residues 240–293 were analyzed with HELIQUEST (62) as canonical α-helices. The activities were assayed using the standard conditions in the absence and presence of saturating concentrations of egg PC/PG (1:1) *small unilamellar* vesicles. The ratio of these two values (±lipid) for each mutant was plotted as a function of domain M hydrophobicity (*top panel*; $R^2 = 0.91$) or helical hydrophobic moment (*bottom panel*; $R^2 = 0.90$). The data in *panel E* are means ± S.D. of at least three independent determinations. Maximal lipid-stimulated activity values for these variants ranged from 35 to 100% of fully active CCT-367.

Upon loss of the segment between residues 312 and 271, k_{cat} values for the CCT soluble form transitioned from silenced (0.5 s^{-1}) to the partially active rate (~ 3 s^{-1}) characteristic of CCT-236 (Fig. 1*B*). The construct ending at residue 271 showed a higher k_{cat} than did CCT-255 or CCT-236, perhaps reflecting different consequences of specific truncation sites on protein dynamics. Loss of the AI segment was linked to a transition in the CTP K_m from ~9 to ~5.5 mM (Fig. 1*C*). Thus, the presence of the AI segment suppresses k_{cat}/K_m by about 10-fold. However, the kinetic parameters of the full-length soluble enzyme were achieved only when the segment between residues 293 and 312 was intact. These results strengthen previous results implicating a key silencing role for the AI motif (16) but suggest additional participation of the flanking segment between residues 293 and 312. For comparison, fully active, membrane-bound CCT (CCT_{mem}) features a k_{cat} value of ~13 s^{-1} and a K_m of 0.5–1 mM.

The Hydrophobicity and Amphipathy of the AI Segment Are Important for Silencing Function—The most conserved feature of the AI segment is the spacing of hydrophobic residues, which tend to be aromatic and/or bulky (Fig. 1*D*). The effects of substitution of sets of these to alanine or serine on the lipid-independent specific activities (expressed as a fraction of maximal activity obtained with saturating concentrations of lipid) of full-length CCT constructs (CCT-367) are shown in Fig. 1*E*. As the hydrophobicity of domain M was reduced by mutation, the fractional lipid-independent activity increased from 0.03 (WT CCT-367) to 0.18 (CCT-367(10S). Thus, silencing function

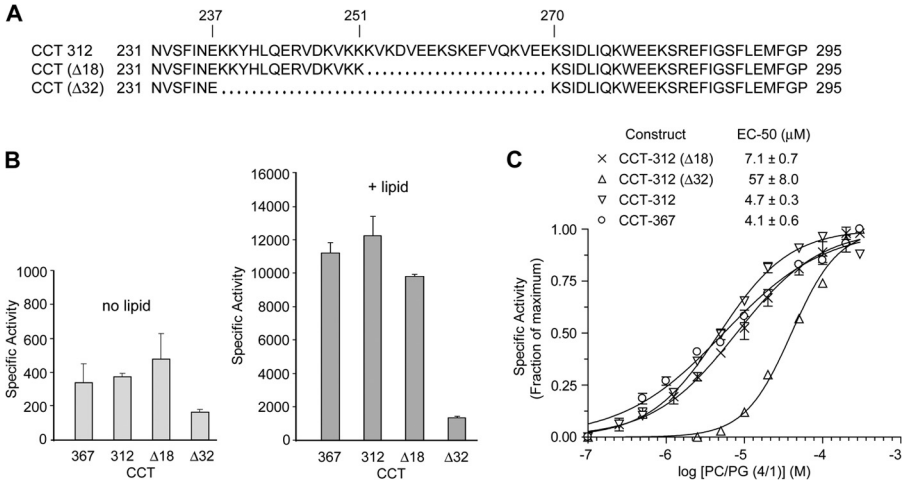

FIGURE 2. **Specific activity of CCT-312 and constructs with leash deletions.** *A*, domain M sequences of CCT-312 and deletion mutants. *B*, the specific activities of the various purified CCTs were determined using the standard assay. CCT-367 refers to full-length WT CCT. The lipid vesicles were composed of egg PC/egg PG (1:1). Note the *y axis* scales differ by 10-fold in the two graphs. Data are means ± range of two independent experiments. *C*, standard activity assay in the presence of variable egg PC/egg PG (4:1) vesicles. The *error bars* in *panel C* represent the range of duplicate determinations. The data were fit to models, and the V_{max} and EC_{50} values were obtained using GraphPad Prism.

TABLE 1

Data collection, molecular replacement, and refinement statistics

ASU, asymmetric unit; Ave., average. The data collection statistics in parentheses are the values for the highest resolution shell.

	CCT-312 crystal[a]	CCT-312(Δ32) crystal
Data collection		
Wavelength (Å)	1.105	0.979
Space group	$P4_3$	$P2_1$
a, *b*, *c* (Å)	107.78, 107.78, 575.71	87.26, 44.55, 97.13
α, β, γ (°)	90.0, 90.0, 90.0	90.0, 111.21, 90.0
Resolution (Å)	107.8–8.0 (8.4–8.0)	40.0–3.0 (3.16–3.0)
R_{merge}	0.18 (0.66)	0.14 (0.34)
R_{pim}	0.08 (0.28)	0.09 (0.21)
Completeness (%)	100 (100)	92.2 (92.3)
Total reflections	45,866 (6,780)	45,086 (6,561)
Unique reflections	6,964 (1,018)	13,084 (1,901)
Multiplicity	6.6 (6.7)	3.4 (3.5)
Mean $(I)/\sigma(I)$	9.3 (3.0)	7.0 (3.3)
Average mosaicity	1.0	1.9
Refinement statistics		
Refinement method	Rigid body	PHENIX restrained
Protein molecules in ASU	8	2
Water molecules		21
Protein residues	2,021	432
Total number of atoms	10,256	3,202
R_{work}/R_{free}	0.38/0.41	0.22/0.29
Ave. *B*-factor (all atoms) (Å^2)	32.5	35.40
Ave. *B*-factor (CDP-choline) (Å^2)		32.05
r.m.s.d. bond angles (°)		0.96
r.m.s.d. bond length (Å)		0.004
Ramachandran plot		
Most favored (%)	97.6	95.3
Additionally allowed (%)	2.4	4.8
Disallowed (%)	0.0	0.0
PDB ID code	4MVD	4MVC

[a] The initial solution for the CCT-312 diffraction set was obtained using CCT-236 structure (Protein Data Bank code 3HL4) as a search model. Subsequent to the solution of the 3-Å CCT-312(Δ32) structure (Protein Data Bank code 4MVC), it was used as the search model for the 8-Å data set for CCT-312, which afforded a better fit to the experimental density. The parameters in this table are derived from the latter process.

clearly correlates with hydrophobicity of the AI. Silencing function also correlated with the amphipathy value (Fig. 1*E*, *lower panel*), consistent with an amphipathic helix structure for the AI motif. The fractional lipid-independent activity for CCT-367(10S) was only 0.18 compared with 0.27 for a CCT with a deletion of the entire AI segment (16) or 0.44 for CCT-271 truncated just before the AI motif. These data suggest that although the hydrophobic residues within the AI segment contribute to catalytic silencing there are likely other interactions that participate.

The Crystal Structures of CCT312 and CCT-312(Δ32) Show a Four-helix Bundle Interaction Involving the AI and αE Helices—To understand the mechanism for silencing by the AI segment, we sought to obtain the structure of CCT-312. CCT-312, which is missing only the disordered phosphorylation (P) region, has catalytic and regulatory properties similar to full-length CCT

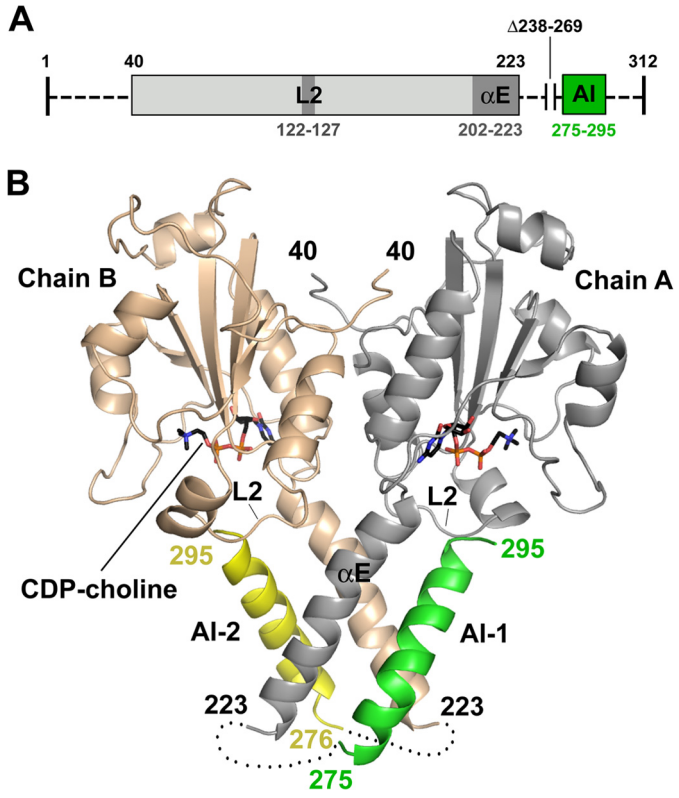

FIGURE 3. **Structure of CCT-312(Δ32) dimer reveals the interactions of the AI segment with αE helices and loop L2.** *A*, in the schematic diagram, the resolved portions of each monomer are shown in *boxes*, and unresolved portions are in *dashed lines*. *B*, structure of residues 40–223 and the AI segments (residues 275(276)–295). The linkers between the end of the αE helices and the start of the AI helices are unresolved. CDP-choline is shown in *stick* presentation.

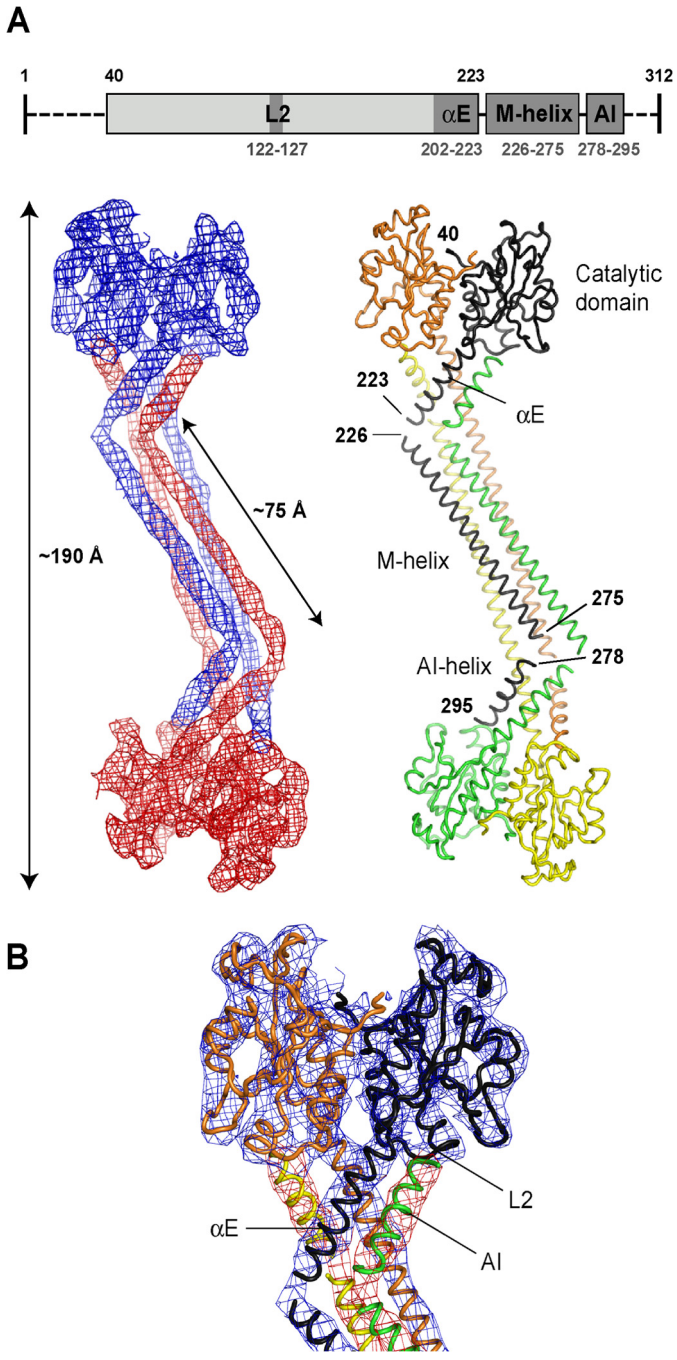

FIGURE 4. **Refined electron density at 8-Å resolution and model for CCT-312 tetramer.** *A*, *top panel*, in the schematic diagram, the resolved portions of each monomer are indicated by *boxes*, and unresolved segments are in *dashed lines*. *Bottom panel*, refined molecular replacement solution using the 3-Å CCT-312(Δ32) as the search model. The ($2F_o - F_c$) electron density map corresponding to a tetramer is shown with two dimers colored *blue* and *red* at 1.5 σ. The model is composed of four separate chains (*black*, *orange*, *green*, and *yellow*). Structural elements are labeled for the *black* chain (chain A). *B*, close-up of the catalytic domain shows the positioning of the C-terminal AI-1 segment (*green*) antiparallel to the helix αE (*black*) and its end (estimated to be Pro^{295}) immediately adjacent to loop L2 (*black*). A nearly identical structural model was generated using CCT-236 as the search model and subsequent refinement.

(Ref. 22 and Figs. 1, *B* and *C*, and 2). Extensive screens with CCT-312 generated only poorly diffracting crystals, one of which generated an 8-Å diffraction data set. To obtain crystals with better diffraction quality, we screened CCT-312 variants with various deletions from the disordered leash portion of domain M. Deletion of the 18-residue (residues 252–269) non-conserved portion of the leash (CCT-312(Δ18)) had minimal impact on silencing or lipid activation (Fig. 2), indicating that this portion of the leash is dispensable for regulation of activity. However, crystallization trials were unsuccessful. CCT-312(Δ32) missing 32 residues (residues 238–269) from both the non-conserved and polybasic sections of domain M readily crystallized in the presence of CDP-choline. This construct showed strong silencing in the absence of lipid and partial activation in the presence of excess lipids (Fig. 2*B*). The lack of full activation is likely because the abbreviated M domain only weakly binds the membranes. Titrations with PC/PG (4:1) vesicles showed equivalence among CCT-367, CCT-312, and CCT-312(Δ18) but a 10-fold higher EC_{50} for CCT-312(Δ32) (Fig. 2*C*).

A CCT-312(Δ32) crystal generated a 3-Å resolution diffraction data set that was solved by molecular replacement using CCT-236 (Protein Data Bank code 3HL4) (see Table 1). The asymmetric unit was a dimer. The resolved portion of this dimer encompasses the catalytic domains and the AI segments of domain M (Fig. 3*A*). The segments linking the end of the αE helices to the AI helices are not resolved, which is indicative of their disorder. Because of this, there is uncertainty in assigning the two AI helices to chain A or B. We refer to them as AI-1 (resolved residues 275–295) and AI-2 (resolved resi-

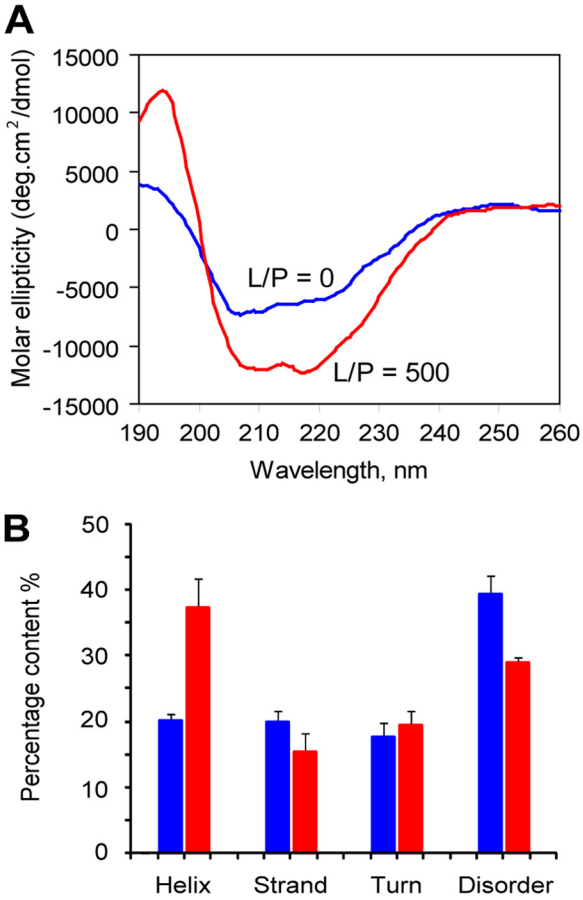

FIGURE 5. **CD analysis of the secondary structure of CCT-312.** *A*, CD spectra of CCT-312 (2 μM) in phosphate buffer without or with lyso-PC/egg PG (4:1, mol/mol) micelles. *L/P*, lipid/protein molar ratio; *deg*, degrees. *B*, deconvolution of the CD spectra shown in *A* by CDPro. The average percent secondary structure ±S.D. for the results of three separate deconvolution programs within the CDPro suite is shown. *Blue bars*, no lipid; *red bars*, +lipid. The analyses were repeated on a separate preparation of CCT-312 with very similar results.

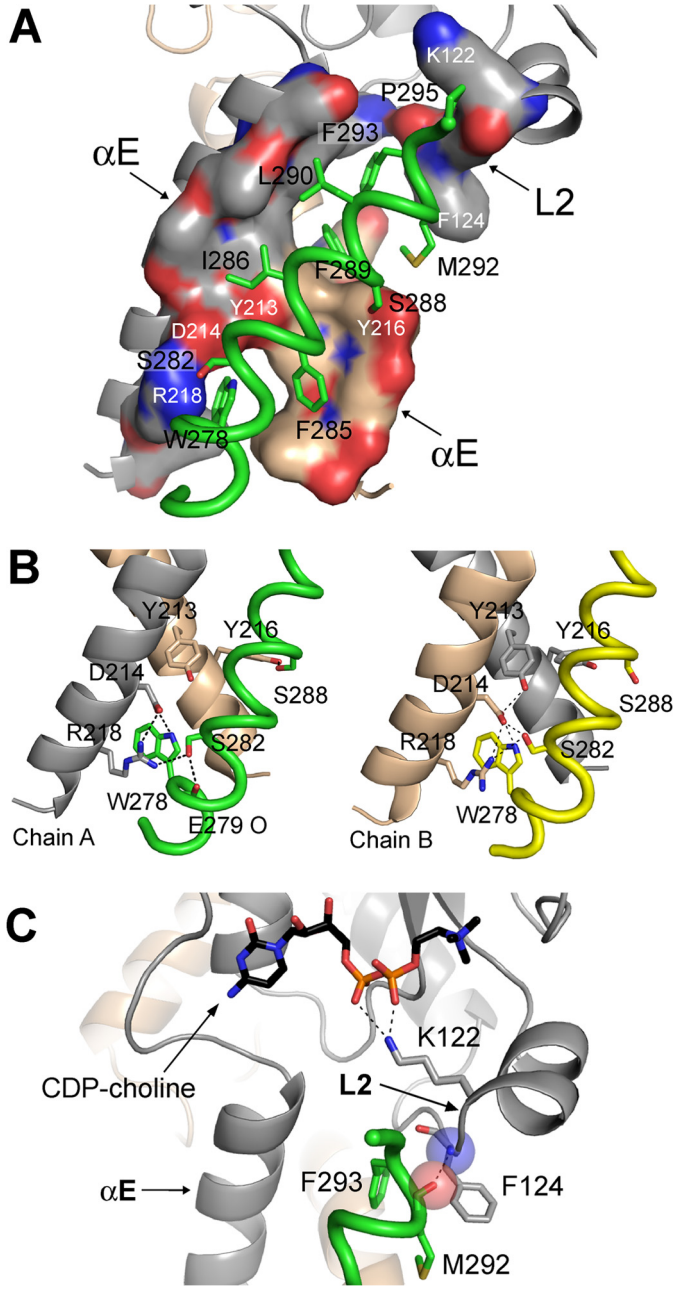

FIGURE 6. **Specific contacts between the AI segment and αE helix/loop L2 in the catalytic domain.** *A*, position of residues in one AI helix that engage the binding site on the catalytic domain. Residues contributed by AI and αE are shown in *black* and *white*, respectively. Chain A, *gray*; chain B, *wheat*. *B*, asymmetry in the network of polar interactions at the base of the AI-αE bundle. *Left panel*, AI-1 (*green*); *right panel*, AI-2 (*yellow*). *C*, interactions at the AI-L2 interface involve backbone contacts. The H-bond between the Met^{292} carbonyl (*pink sphere*) at the C terminus of the AI helix (*green*) with the NH at Phe^{124} (*blue sphere*) in loop L2 is highlighted. See also Tables 2 and 3.

dues 276–295) (see Fig. 3*B*). Each AI helix interacts with both αE helices, and together they form an antiparallel four-helix bundle near the opening of the active site. The two AI segments have very similar conformations with a bend at Lys^{281}. AI-2 is unraveled between residues Gln^{276} and Trp^{278}. Each AI helix ends in a sharp turn at ^{294}GP (the AI-turn), which interacts with loop L2 at the mouth of the active site (discussed below).

The AI positioning in the CCT-312(Δ32) structure is not an artifact of the large domain M deletion. A very similar AI-αE-L2 interaction is found in CCT-312 with no deletion. We initially used the 2.2-Å CCT-236 structure and subsequently the 3.0-Å CCT-312(Δ32) structure as a search model for the 8.0-Å data set of CCT-312. Both yielded very similar molecular replacement solutions and refined models (Fig. 4 and Table 1). But there were significant statistical improvements using CCT-312(Δ32), indicating that the CCT-312(Δ32) structure was the more accurate search model. This suggests that the positioning of the AI segments in the CCT-312(Δ32) structure reflects the positioning of those of the CCT-312 with a complete M domain.

Unexpectedly, the refined CCT-312 structure revealed a tetrameric complex (a dimer of dimers) with the M domains in mostly full α-helical conformation extending directly from the αE helices of one catalytic dimer to the active site of another dimer (Fig. 4). The M helices of the two dimers interact to form a very long and loose antiparallel four-helix bundle. Gel filtration of this same preparation of CCT-312 showed a mixture of dimer and tetramer species. CD analysis showed a large increase in helical content (~52 residues) induced by lipid

TABLE 2

Interactions among the AI, αE, and L2 segments

Residues in the interacting face of the AI-1 segment are listed in column 1, and the residues in the catalytic domain with atoms located within 4 Å of each AI-1 residue are listed in the other columns. For the AI-2 segment the residues on each chain would be the reverse. Except where noted (*,**), all interactions are side-chain van der Waals contacts. *, Hydrogen bonding side-chain interaction. **, Interaction between backbone atoms.

		αE helices	
AI segment 1	L2 chain A	Chain A	Chain B
Pro^{295}	Lys^{122}		
Gly^{294}	Lys^{122}		
Phe^{293}	Phe^{124}, Val^{126}	Ile^{206}	
Met^{292}	Gly^{123}, Phe^{124}**, Phe^{124}		Tyr^{216}
Leu^{290}		Ser^{203}, Ile^{206}, Thr^{207}	
Phe^{289}		Val^{210}	Ile^{209}, Asp^{212}, Tyr^{213}, Tyr^{216}
Ser^{288}*			Tyr^{216}*
Ile^{286}		Thr^{207}, Val^{210}, Arg^{211}	Tyr^{213}
Phe^{285}			Tyr^{213}, Ala^{217}, Asn^{220}, Leu^{221}
Ser^{282}*		Arg^{218}*	
Trp^{278}		Asp^{214}*, Arg^{218}, Leu^{221}	Ala^{217}, Leu^{221}

TABLE 3

Polar interactions between the αE helices and AI helices

The interactions are non-equivalent for the two AI segments.

AI-1	Helix αE	Å	AI-2	Helix αE	Å
Ser^{288} Oγ	Tyr^{216} OH[a]	2.4			
Ser^{282} Oγ	Arg^{218} Nη1	3.6	Ser^{282} Oγ	Arg^{218} Nη2	3.3
				Asp^{214} Oδ2	2.5
Trp^{278} Nε1	Asp^{214} Oδ1	2.6	Trp^{278} Nε1	Asp^{214} Oδ1	3.0
	Arg^{218} Nη1	3.8		Asp^{214} Oδ2	3.8
Trp^{278} O	Arg^{218} Nη1	3.2			

[a] Residue in helix αE of the opposite chain.

micelles (Fig. 5). These data suggest that in solution the dominant CCT-312 dimeric form has mostly disordered M domains and is refractory to crystallization and that only the tetrameric species with its ordered M domains was amenable to crystallization in the given condition. Despite the unexpected M domain arrangement, in both refined tetrameric models, the density for the C-terminal ~15 residues of each M helix rests against the αE helices and terminates at the L2 loop. We can assign these terminal residues to the AI segment as the density can be traced continuously from αE as an extended M helix of known sequence (Fig. 4).

The AI-αE Helical Interaction Involves Hydrophobic and Polar Contacts—Two αE helices and loop L2 create a shallow elongated binding cavity for each AI segment. The residues contributing to the cavity are indicated in Fig. 6*A* and Table 2. The αE helices are longer than observed in the structure of CCT-236 where the visible density ended at residue 215 (chain A) or 216 (chain B) (7). This suggests stabilization of the αE helices by the interacting AI helices. The AI helix, an amphipathic helix with a conserved hydrophobic face and a less conserved polar face, uses the αE hydrophobic cavity to bury its aromatic residue-rich non-polar face. The mutagenesis results of Fig. 1*E* support a silencing function for these interactions. The specific contacts between residues in the AI and αE helices are described in Tables 2 and 3. The van der Waals interface between the helices is rather loose, featuring ridges-into-grooves packing involving mostly bulky side chains. There are no αE-AI packing interactions involving backbone contacts. In total, 30 hydrophobic side chains, including 12 aromatic side chains, are sequestered partially or fully away from water in the formation of the αE-AI four-helix bundle (Table 2). Most of the charged side chains in the AI segment facing the solvent did not have strong densities, reflecting the absence of constraining interactions.

Although the interacting surfaces in the four-helix bundle that forms from two αE and two AI helices are mainly hydrophobic, there is a network of polar interactions near the base of the bundle (Fig. 6*B*). Both AI helices feature Trp^{278} and Ser^{282} contacts with the αE residues Asp^{214} and Arg^{218}, respectively. However, there is variation in the H-bonding network in AI-1 *versus* AI-2 due to different side chain rotamers for Asp^{214}, Ser^{282}, and Ser^{288}. In AI-1, Ser^{288} makes a novel H-bond to Tyr^{216} in αE of chain B. In AI-2, Ser^{282} makes a novel H-bond to Asp^{214} in αE of chain B (Fig. 6*B* and Table 3). Thus, there may be more than one low energy binding interaction between the AI and the αE, and two have been captured in our structure.

The AI Segment Makes Direct Contact with Loop L2—The C-terminal end of the AI helix and AI-turn at ^{292}MFGP^{295} is juxtaposed with residues ^{122}KGF^{124} of loop L2 (Fig. 6*C*). The backbone of the AI helix-turn at Met^{292}, Phe^{293}, and Gly^{294} are within H-bonding distance of backbone atoms at Phe^{124} and Lys^{122} in loop L2 (Table 2). At the C terminus of the AI helix, the interaction surface contributed by the catalytic domain is sparse. Two hydrophobic residues at the end of the AI helix, Met^{292} and Phe^{293}, interface only loosely with the side chain of Phe^{124} in L2. The bulky side chain of Tyr^{216} in helix αE may serve to guide the AI helix-turn to contact the L2 loop.

The Architectures of the CCT-312(Δ32) and CCT-236 Active Sites Are Similar—An overlay of the active sites of the partially active CCT-236 (Protein Data Bank code 3HL4) and the totally silenced CCT-312(Δ32) are surprisingly similar (Fig. 7*A*). We were anticipating that at a minimum in CCT-312(Δ32) the L2 loop would be displaced to realign Lys^{122}. One explanation for the similarity is that the bound CDP-choline ligand can dictate the positions of the active site residues, essentially overriding the effects of the bound AI helix. Active site ordering by CDP-choline is supported by molecular dynamics simulations of CCT-236 with and without CDP-choline (Fig. 7, *B–D*). Root mean square fluctuation analysis of all backbone atoms during a 200-ns simulation revealed high mobility in active site elements L1, L2, L4/αD, and L6/αE (Fig. 7*B*). A CDP-choline stabilizing effect was observed for these mobile elements except for the C-terminal portion of helix αE, which unraveled in both simulations (Fig. 7, *B* and *C*). Stabilization was most pronounced for loop L2 (Fig. 7, *C* and *D*). During the simulation in the absence

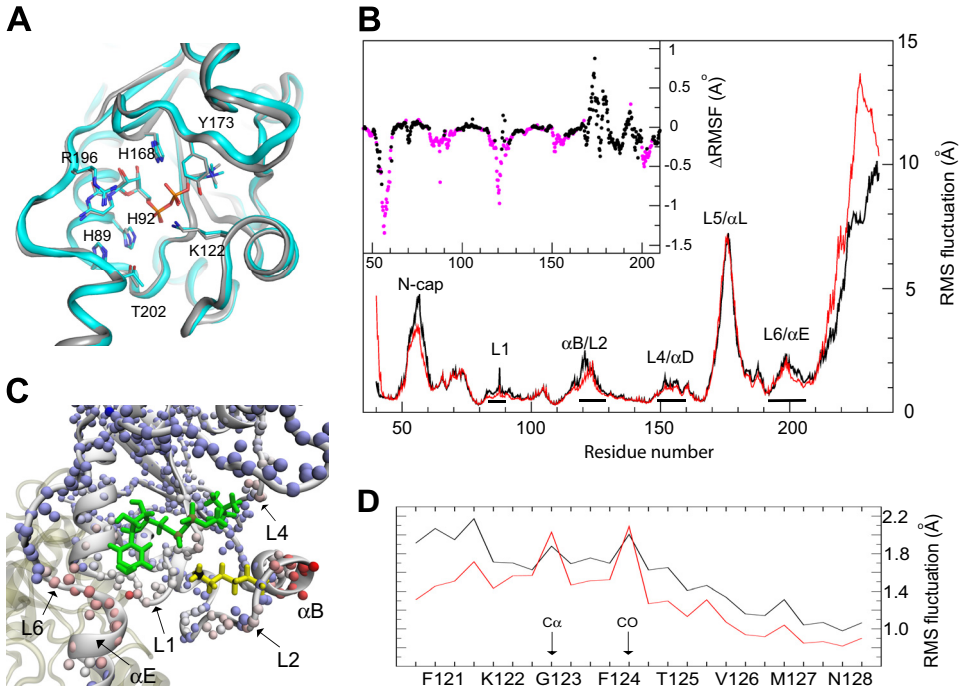

FIGURE 7. **Similarity of active site architecture between silenced and desilenced CCT may be due to the ligated CDP-choline.** *A*, overlay of the active sites of CCT-312(Δ32) (*gray*) and CCT-236 (*cyan*; Protein Data Bank code 3HL4). Key active site residues are labeled, and CDP-choline is in the central cavity. *B–D*, MD simulations. *B*, fluctuation analysis of all backbone atoms of CCT-236 in the absence (*black line*) and presence of CDP-choline (*red line*). Mobile active site structural elements are displayed as *bars* above the sequence. Data are from 40,000 5-ps frames and show the average root mean square (*RMS*) fluctuation (*RMSF*) over a 200-ns simulation using GROMACS 4.6. The CCT in each frame was aligned to the stable β-sheet backbone of both subunits to eliminate effects of whole molecule translation and rotation. The *inset* reports the difference in average fluctuation between the two sets, and statistically significant Δ values are in *magenta*. *C*, image of the CCT-236 catalytic dimer color-coded on one subunit to show the effects of CDP-choline on the root mean square fluctuations of backbone atoms. *Blue*, no effect or small destabilization by CDP-choline. *Blue → white → red* represents the degree of stabilization afforded by CDP-choline (*green*); stabilized elements are labeled. The side chain of Lys^{122} is shown in *sticks* (*yellow*). The image was generated using VMD software and the data in *B*. *D*, fluctuation analysis of the backbone atoms of loop L2 over 200-ns simulation time in the absence (*black*) or presence (*red*) of CDP-choline.

of CDP-choline, the active site residues Arg^{196} (L6) and Lys^{122} (L2) quickly reoriented from their starting position (facing the phosphates of the CDP-choline) to more solvent-exposed positions. The lysine side chain then fluctuated through many orientations during the simulation. In the presence of CDP-choline, Lys^{122} remained pointing into the active site during the entire 200 ns. The backbone fluctuations in loop L2 were reduced for the entire loop in the presence of CDP-choline with the exception of backbone atoms at the Gly^{123} Cα and Phe^{124} carbonyl carbon (Fig. 7*D*). If CDP-choline can dictate the arrangement of the active site, then a ligand-free structure might reveal a more accurate effect of the bound AI segment.

MD Simulations Reveal That the AI Helix Forges Interactions with Loop L2 That Constrain Lys^{122} Orientations—Simulations of the CCT-312(Δ32) dimer were performed using starting structures with the AI helices present or removed. The ligand CDP-choline was not included in the 210-ns simulations. For both simulations, fluctuation analysis of all backbone atoms revealed high mobility in the active site loops and helix αE as in the simulations of CCT-236. We focused on AI-dependent changes in the αE helices and L2 loop as these form the AI binding site in the solved structures. In the absence of the AI segments, portions of the αE helices unraveled locally within 20 ns and did not reform over the duration of the simulation. In the simulations with the AI segments included, the AI helices remained bound to the αE helices to maintain a stable bundle of four α-helices. As a result, the AI-turn remained in contact with loop L2 for the full duration. In the presence of the AI, the dynamics of the loop L2 backbone, monitored as root mean square deviation (r.m.s.d.) from the starting structure, showed a ~1-Å reduction in r.m.s.d. and a dramatic reduction in fluctuations (Fig. 8*A*). The restraining interaction of the AI-turn on L2 was mediated by backbone contacts as in the crystal structure and by side chain interactions between Phe^{124} in L2 and Met^{292} and Phe^{293} in the AI helix.

This AI-turn-L2 interaction had profound consequences on the orientation of the Lys^{122} side chain. During the simulation without the AI segment, the Lys^{122} side chain sampled multiple, but preferred, orientations (Fig. 8*B*). In the first ~60 ns of the simulations with the AI helices, the Lys^{122} side chains at both active sites forged intermittent interactions with the backbone of the AI-turn. Then between 60–70 ns, the hydrophobic pair, Phe^{293} in the AI helix-turn and Phe^{124} in the L2 loop, assumed new rotameric states that resulted in a more intimate contact between them and positioned their carbonyl oxygens for interaction with the Lys^{122} ϵ-amino (Fig. 8, *C* and *D*). This interaction remained intact for the duration of the simulation in chain B and for ~20 ns in chain A. The Lys^{122} side chain positioning continued to be constrained in chain A by a fluctuating contact primarily with the Phe^{293} carbonyl. Thus, the Lys^{122} side chain became trapped in a more stable polar interaction with the

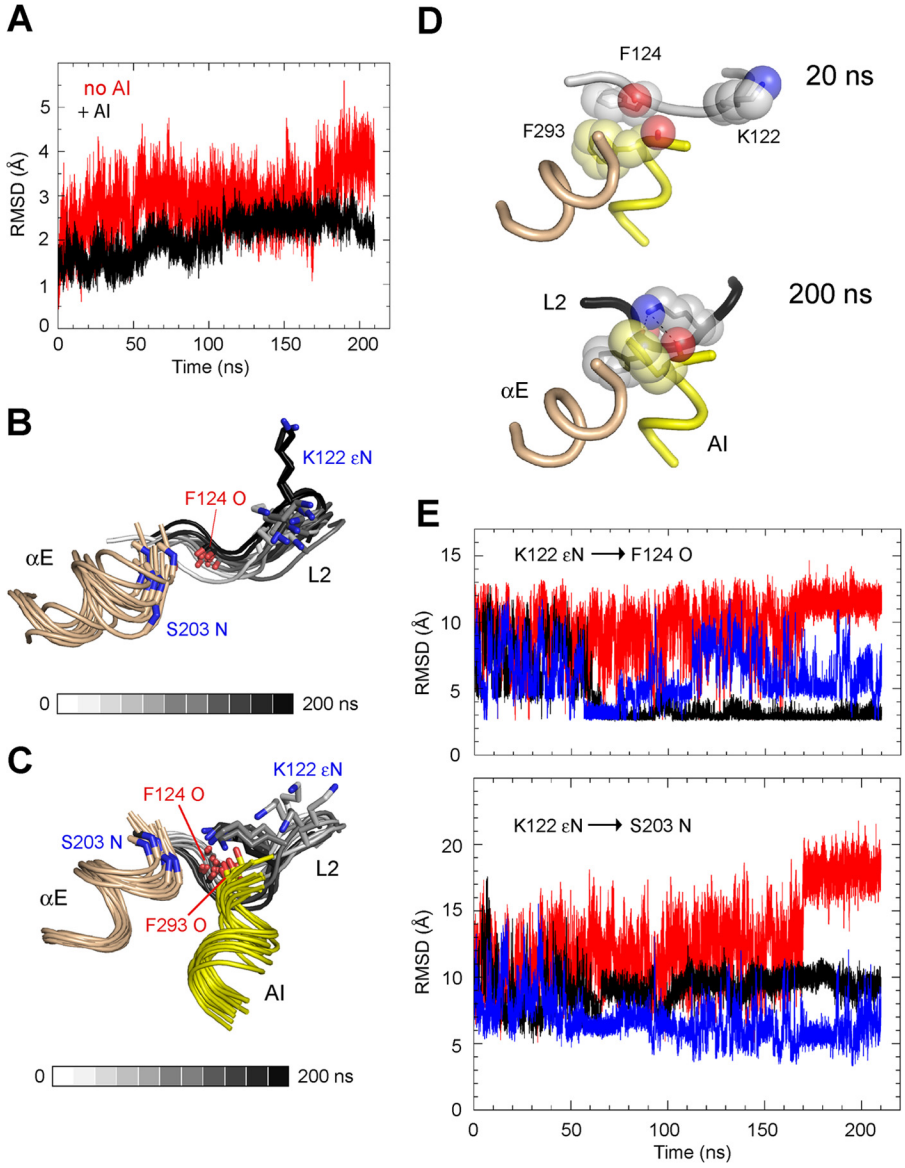

FIGURE 8. **MD simulations of CCT-312(Δ32).** The effect of AI segment on loop L2 and Lys^{122} dynamics is shown. *A*, r.m.s.d. analysis of the ensemble of all atoms of the loop L2 backbone (residues 121–128) in the absence (*red*) or presence (*black*) of the AI segments. The analysis without the AI included 24 atoms from chain A. Chain B analysis was discarded because in the absence of the AI the unraveled αE inserted into the mouth of the active site, constraining the dynamics of L2. The analysis with the two AI segments included both chains (48 atoms). *B* and *C*, snapshots showing the time-dependent change in orientation of Lys^{122}. Structures captured every 20 ns were overlaid in PyMOL to show positional change during the 210-ns simulation. *B*, no AI. *C*, with AI-2 (Gln^{276}–Pro^{295}). Loop L2 and Lys^{122} positional shift is denoted by *shades* of *gray*. *D*, repositioning of Phe^{293} and Phe^{124} accompanies the formation of a polar interaction between Lys^{122} ϵ-amino and the backbone carbonyls at these phenylalanines. This interaction in chain B is stable for >130 ns. *E*, time-dependent distance analysis (obtained using VMD software) between the ϵ-amino atom of Lys^{122} and two backbone atoms near the docked AI helix-turn, Phe^{124} carbonyl oxygen in loop L2 (*top panel*) and Ser^{203} nitrogen in the N terminus of the αE helix (*bottom panel*). The positions of these backbone atoms are shown in *B* and *C*. *Red*, no AI present; analysis on chain A only; *blue*, analysis of chain A with AI-1 bound; *black*, analysis of chain B with AI-2 bound.

AI-turn. These effects of the AI on the dynamics and positioning of Lys^{122} were also revealed in an analysis of the distance fluctuations over time between two backbone atoms located in the vicinity of the AI-turn: the Phe^{124} carbonyl oxygen and Ser^{203} amide nitrogen (Fig. 8*E*). The effects are consistent with a movement of the Lys^{122} side chain and ϵ-amino group toward the AI-turn where it localizes between the carbonyls of Phe^{293} in the AI-turn and Phe^{124} in the L2 loop.

DISCUSSION

Of the many enzymes that have autoinhibitory domains that double as membrane-binding motifs, there are only a few for which the switching mechanisms between silenced and activated states are understood at a detailed structural level, including the protein kinases PKC and PKB and the GTPase exchange factors β2-chimerin and Grp1 (1, 46–48). These proteins use modules that bind a lipid monomer within the membrane, such as C1 domains for diacylglycerol or pleckstrin homology domains for phosphatidylinositol 4,5-bisphosphate. Among the class of amphitropic proteins that rely *exclusively* on lipid-induced amphipathic helices for membrane binding, the switch mechanism has been elucidated at the atomic level only for pyruvate oxidase from *Escherichia coli* (49, 50). In that enzyme, the autoinhibitory C-terminal 40 residues take on a mixed

α/β + extended tail structure that occludes most of the active site and dislocates a key active site residue, Phe^{465}, that in the activated form likely mediates electron transfer between bound cofactors (49). This inhibitory structure reorganizes to form a linker and an amphipathic helix in the membrane-bound state (50). Our analysis of CCT suggests an autoinhibition mechanism, like that of pyruvate oxidase, involving substrate occlusion and dislocation of a key active site residue, but there are also substantial differences, such as the intrinsically disordered nature of a large portion of the regulatory M domain.

The mechanism of autoinhibition by the CCT domain M that is emerging involves an ordered, autoinhibitory amphipathic helix on a flexible leash. A structureless leash, suggested by previous spectroscopic evidence (19–21), is supported by the lack of density for domain M residues outside of the AI helix in our 3.0-Å structure of the CCT-312(Δ32) dimer. Although the CCT-312 tetrameric structure showed an ordered helical conformation for the entire M domain, we have argued above that this represents a minor conformer in the ensemble that was more amenable to crystallization. The leash does not directly mediate catalytic silencing as deletion of 18 leash residues did not increase lipid-independent activity. The αE-AI silencing interaction, previously based on low resolution methods (16, 21), is strengthened by the interactions revealed in both new x-ray-derived structures.

The major autoinhibition mechanisms that have been elucidated for allosteric enzymes include (*a*) direct steric block of active sites using pseudosubstrate motifs (51) or unoccupied ligand binding domains (46), (*b*) allosteric clamping of the active site in "closed" or non-productive configurations by unoccupied ligand binding domains (47, 52), and (*c*) disabling of the active site by dislocating a key substrate-binding element (46, 53). There is also evidence that allosteric mechanisms can impact protein dynamics without a change in structure (54). Our data are compatible with a combination of these strategies contributing to autoinhibition by the CCT AI helix.

The rate-limiting step in the overall catalytic mechanism is not known for CCT. The reduction in k_{cat}/K_m by the AI helix-turn implies an impact on the rate associated with the capture of substrate into a productive ES complex, but the product release step could also be inhibited by the AI helix-turn. Fig. 9 illustrates how the opening to the active site is partly covered when the AI segment binds to the αE helices; thus, substrate access and/or product release could be restricted. The interaction of the AI helix-turn with loop L2 is also likely to contribute to its inhibitory mechanism by clamping L2 in a non-productive orientation and/or by constraining its dynamics. This interaction is backbone to backbone and may be stabilized by a cluster of hydrophobic interactions involving residues from the AI-turn and L2 in addition to the stable four-helix bundle. Molecular dynamics simulations probing the effect of the bound AI segment support a role for this hydrophobic cluster. We propose that this interaction impedes loop L2 movements and constrains the conformational space of the key catalytic residue on loop L2 during a catalytic cycle.

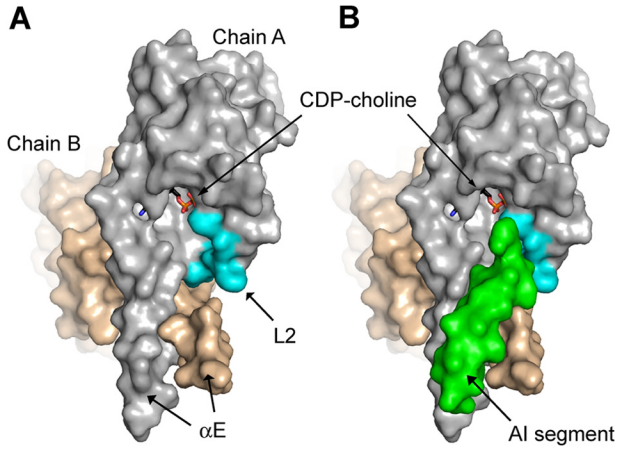

FIGURE 9. **The AI segment occludes part of the opening to the active site.** Chain A of CCT-312(Δ32) (*gray*) and its active site is shown with chain B (*wheat*) in surface rendering without (*A*) and with (*B*) the docked AI segment-1 (*green*). Loop L2 is in *cyan*.

The evidence for loop L2 movement during a catalytic cycle is from a comparison of bacterial glycerol-phosphate cytidylyltransferase structures with CTP bound *versus* CDP-glycerol product bound that revealed a ~3-Å displacement of loop L2 backbone into the active site to engage the product (55). This loop closure may facilitate the transition state by bringing the ϵ-amino group of the Lys^{122} analog into contact with both the α-phosphate of CTP and the phosphate oxygen of the attacking nucleophile (55). It would also exclude water, optimizing the electrostatic interactions between the anionic substrates and basic active site groups (56). After the reaction, loop L2 would open to release product. The interaction of the AI-turn could hamper any of these loop movements.

Spectroscopic measurements of active site loop closure and opening dynamics have yielded correlation times ranging from ns to hundreds of μs (56–60). The time scale of the MD simulations we conducted (200 ns) did not capture the full L2 loop displacement. However, the simulations did reveal a profound and unanticipated effect of the AI-L2 interaction on the positioning of Lys^{122}: the AI-L2 contact reorganizes a cluster of hydrophobic residues contributed from both segments that stabilizes a polar contact between the Lys^{122} ϵ-amino and a backbone atom of the AI-turn. Whether this trap for the catalytic lysine would impact its interaction with substrates will be probed by additional simulations in the presence of individual substrates and products.

Our analysis thus far suggests a plausible silencing mechanism that explains the effect of the AI helix-turn on the development of a kinetically productive ES complex leading to product formation (k_{cat}/K_m). Displacement of the AI segment upon engagement with membranes would disrupt the inhibitory interaction that blocks the opening to the active site and constrains the movements of loop L2 and Lys^{122}.

CCT is up-regulated in *ras*-transformed epithelial cells and is required for maintaining transformed cells in an anoikis-resistant state (61), a prerequisite for metastasis. Establishing the mechanism of autoinhibition of CCT is important for developing inhibitors based on the AI motif that might be developed as potential suppressors of metastasis.

Acknowledgments—We thank Dr. Mark Paetzel for use of equipment for purification and initial diffraction collection and for helpful advice. We are grateful to Ziwei Ding for construction of many plasmids and to Deidre de Jong-Wong for valuable technical assistance. Simulations used West-Grid/Compute Canada facilities. Diffraction was obtained at Beamlines 081D-1 and 08B1–1 at the Canadian Light Source, which is funded by the Canada Foundation for Innovation, the Natural Sciences and Engineering Research Council of Canada, the National Research Council Canada, the Canadian Institutes of Health Research, the Government of Saskatchewan, Western Economic Diversification Canada, and the University of Saskatchewan.

REFERENCES

1. Leonard, T. A., and Hurley, J. H. (2011) Regulation of protein kinases by lipids. *Curr. Opin. Struct. Biol.* **21,** 785–791
2. Cornell, R. B., and Northwood, I. C. (2000) Regulation of CTP:phosphocholine cytidylyltransferase by amphitropism and relocalization. *Trends Biochem. Sci.* **25,** 441–447
3. Tian, Y., Zhou, R., Rehg, J. E., and Jackowski, S. (2007) Role of phosphocholine cytidylyltransferase alpha in lung development. *Mol. Cell. Biol.* **27,** 975–982
4. Jacobs, R. L., Devlin, C., Tabas, I., and Vance, D. E. (2004) Targeted deletion of hepatic CTP:phosphocholine cytidylyltransferase α in mice decreases plasma high density and very low density lipoproteins. *J. Biol. Chem.* **279,** 47402–47410
5. Krahmer, N., Guo, Y., Wilfling, F., Hilger, M., Lingrell, S., Heger, K., Newman, H. W., Schmidt-Supprian, M., Vance, D. E., Mann, M., Farese, R. V., Jr., and Walther, T. C. (2011) Phosphatidylcholine synthesis for lipid droplet expansion is mediated by localized activation of CTP:phosphocholine cytidylyltransferase. *Cell Metab.* **14,** 504–515
6. Sarri, E., Sicart, A., Lázaro-Diéguez, F., and Egea, G. (2011) Phospholipid synthesis participates in the regulation of diacylglycerol required for membrane trafficking at the Golgi complex. *J. Biol. Chem.* **286,** 28632–28643
7. Lee, J., Johnson, J., Ding, Z., Paetzel, M., and Cornell, R. B. (2009) Crystal structure of a mammalian CTP:phosphocholine cytidylyltransferase catalytic domain reveals novel active site residues within a highly conserved nucleotidyltransferase fold. *J. Biol. Chem.* **284,** 33535–33548
8. Veitch, D. P., Gilham, D., and Cornell, R. B. (1998) The role of histidine residues in the HXGH site of CTP:phosphocholine cytidylyltransferase in CTP binding and catalysis. *Eur. J. Biochem.* **255,** 227–234
9. Helmink, B. A., Braker, J. D., Kent, C., and Friesen, J. A. (2003) Identification of lysine 122 and arginine 196 as important functional residues of rat CTP:phosphocholine cytidylyltransferase α. *Biochemistry* **42,** 5043–5051
10. Northrop, D. B. (1998) On the meaning of K_m and V/K in enzyme kinetics. *J. Chem. Educ.* **75,** 1153–1157
11. Arnold, R. S., and Cornell, R. B. (1996) Lipid regulation of CTP:phosphocholine cytidylyltransferase: electrostatic, hydrophobic, and synergistic interactions of anionic phospholipids and diacylglycerol. *Biochemistry* **35,** 9917–9924
12. Cornell, R. B., and Taneva, S. G. (2006) Amphipathic helices as mediators of the membrane interaction of amphitropic proteins, and as modulators of bilayer physical properties. *Curr. Protein Pept. Sci.* **7,** 539–552
13. Davies, S. M., Epand, R. M., Kraayenhof, R., and Cornell, R. B. (2001) Regulation of CTP:phosphocholine cytidylyltransferase activity by the physical properties of lipid membranes: an important role for stored curvature strain energy. *Biochemistry* **40,** 10522–10531
14. Johnson, J. E., Xie, M., Singh, L. M., Edge, R., and Cornell, R. B. (2003) Both acidic and basic amino acids in an amphitropic enzyme, CTP:phosphocholine cytidylyltransferase, dictate its selectivity for anionic membranes. *J. Biol. Chem.* **278,** 514–522
15. Johnson, J. E., Rao, N. M., Hui, S. W., and Cornell, R. B. (1998) Conformation and lipid binding properties of four peptides derived from the membrane-binding domain of CTP:phosphocholine cytidylyltransferase. *Biochemistry* **37,** 9509–9519
16. Ding, Z., Taneva, S. G., Huang, H. K., Campbell, S. A., Semenec, L., Chen, N., and Cornell, R. B. (2012) A 22-mer segment in the structurally pliable regulatory domain of metazoan CTP:phosphocholine cytidylyltransferase facilitates both silencing and activating functions. *J. Biol. Chem.* **287,** 38980–38991
17. Friesen, J. A., Campbell, H. A., and Kent, C. (1999) Enzymatic and cellular characterization of a catalytic fragment of CTP:phosphocholine cytidylyltransferase α. *J. Biol. Chem.* **274,** 13384–13389
18. Yang, W., Boggs, K. P., and Jackowski, S. (1995) The association of lipid activators with the amphipathic helical domain of CTP:phosphocholine cytidylyltransferase accelerates catalysis by increasing the affinity of the enzyme for CTP. *J. Biol. Chem.* **270,** 23951–23957
19. Taneva, S., Johnson, J. E., and Cornell, R. B. (2003) Lipid-induced conformational switch in the membrane binding domain of CTP:phosphocholine cytidylyltransferase: a circular dichroism study. *Biochemistry* **42,** 11768–11776
20. Bogan, M. J., Agnes, G. R., Pio, F., and Cornell, R. B. (2005) Interdomain and membrane interactions of CTP:phosphocholine cytidylyltransferase revealed via limited proteolysis and mass spectrometry. *J. Biol. Chem.* **280,** 19613–19624
21. Huang, H. K., Taneva, S. G., Lee, J., Silva, L. P., Schriemer, D. C., and Cornell, R. B. (2013) The membrane-binding domain of an amphitropic enzyme suppresses catalysis by contact with an amphipathic helix flanking its active site. *J. Mol. Biol.* **425,** 1546–1564
22. Dennis, M. K., Taneva, S. G., and Cornell, R. B. (2011) The intrinsically disordered nuclear localization signal and phosphorylation segments distinguish the membrane affinity of two cytidylyltransferase isoforms. *J. Biol. Chem.* **286,** 12349–12360
23. Taneva, S., Dennis, M. K., Ding, Z., Smith, J. L., and Cornell, R. B. (2008) Contribution of each membrane binding domain of the CTP:phosphocholine cytidylyltransferase-α dimer to its activation, membrane binding, and membrane cross-bridging. *J. Biol. Chem.* **283,** 28137–28148
24. Taneva, S. G., Lee, J. M., and Cornell, R. B. (2012) The amphipathic helix of an enzyme that regulates phosphatidylcholine synthesis remodels membranes into highly curved nanotubules. *Biochim. Biophys. Acta* **1818,** 1173–1186
25. Sohal, P. S., and Cornell, R. B. (1990) Sphingosine inhibits the activity of rat liver CTP:phosphocholine cytidylyltransferase. *J. Biol. Chem.* **265,** 11746–11750
26. Cornell, R. B. (1991) Regulation of CTP:phosphocholine cytidylyltransferase by lipids. 2. Surface curvature, acyl chain length, and lipid-phase dependence for activation. *Biochemistry* **30,** 5881–5888
27. Battye, T. G., Kontogiannis, L., Johnson, O., Powell, H. R., and Leslie, A. G. (2011) iMosflm: a new graphical interface for diffraction image processing with MOSFLM. *Acta Crystallogr. D Biol. Crystallogr.* **67,** 271–281
28. Evans, P. (2006) Scaling and assessment of data quality. *Acta Crystallogr. D Biol. Crystallogr.* **62,** 72–82
29. Winn, M. D., Ballard, C. C., Cowtan, K. D., Dodson, E. J., Emsley, P., Evans, P. R., Keegan, R. M., Krissinel, E. B., Leslie, A. G., McCoy, A., McNicholas, S. J., Murshudov, G. N., Pannu, N. S., Potterton, E. A., Powell, H. R., Read, R. J., Vagin, A., and Wilson, K. S. (2011) Overview of the CCP4 suite and current developments. *Acta Crystallogr. D Biol. Crystallogr.* **67,** 235–242
30. McCoy, A. J., Grosse-Kunstleve, R. W., Adams, P. D., Winn, M. D., Storoni, L. C., and Read, R. J. (2007) Phaser crystallographic software. *J. Appl. Crystallogr.* **40,** 658–674
31. Matthews, B. W. (1968) Solvent content of protein crystals. *J. Mol. Biol.* **33,** 491–497
32. Emsley, P., Lohkamp, B., Scott, W. G., and Cowtan, K. (2010) Features and development of Coot. *Acta Crystallogr. D Biol. Crystallogr.* **66,** 486–501
33. Adams, P. D., Afonine, P. V., Bunkóczi, G., Chen, V. B., Davis, I. W., Echols, N., Headd, J. J., Hung, L.-W., Kapral, G. J., Grosse-Kunstleve, R. W., McCoy, A. J., Moriarty, N. W., Oeffner, R., Read, R. J., Richardson, D. C., Richardson, J. S., Terwilliger, T. C., and Zwart, P. H. (2010) PHENIX: a comprehensive Python-based system for macromolecular structure solution. *Acta Crystallogr. D Biol. Crystallogr.* **66,** 213–221
34. Murshudov, G. N., Vagin, A. A., and Dodson, E. J. (1997) Refinement of macromolecular structures by the maximum-likelihood method. *Acta Crystallogr. D Biol. Crystallogr.* **53,** 240–255

35. Sreerama, N., and Woody, R. W. (2000) Estimation of protein secondary structure from circular dichroism spectra: comparison of CONTIN, SELCON, and CDSSTR methods with an expanded reference set. *Anal. Biochem.* **287,** 252–260
36. Vanquelef, E., Simon, S., Marquant, G., Garcia, E., Klimerak, G., Delepine, J. C.., Cieplak, P., and Dupradeau, F. Y. (2011) R.E.D. Server: a web service for deriving RESP and ESP charges and building force field libraries for new molecules and molecular fragments. *Nucleic Acids Res.* **39,** W511–W517
37. Wang, J., Wolf, R. M., Caldwell, J. W., Kollman, P. A., and Case, D. A. (2004) Development and testing of a general Amber force field. *J. Comput. Chem.* **25,** 1157–1174
38. Pronk, S., Páll S., Schulz, R., Larsson, P., Bjelkmar, P., Apostolov, R., Shirts, M. R., Smith, J. C., Kasson, P. M., van der Spoel, D., Hess, B., and Lindahl, E. (2013) GROMACS 4.5: a high-throughput and highly parallel open source molecular simulation toolkit. *Bioinformatics* **29,** 845– 854
39. Lindorff-Larsen, K., Piana, S., Palmo, K., Maragakis, P., Klepeis, J. L., Dror, R. O., and Shaw, D. E. (2010) Improved side-chain torsion potentials for the Amber ff99SB protein force field. *Proteins* **78,** 1950 –1958
40. Jorgensen, W. L., Chandrasekhar, J., Madura, J. D., Impey, R. W., and Klein, M. L. (1983) Comparison of simple potential functions for simulating liquid water. *J. Chem. Phys.* **79,** 926 –935
41. Bussi, G., Donadio, D., and Parrinello, M. (2007) Canonical sampling through velocity rescaling. *J. Chem. Phys.* **126,** 014101
42. Parrinello, M., Rahman, A. (1981) Polymorphic transitions in single crystals: a new molecular dynamics method. *J. Appl. Phys.* **52,** 7182–7190
43. Hess, B., Bekker, H., Berendsen, H. J. C., and Fraaije, J. (1997) LINCS: a linear constraint solver for molecular simulations. *J. Comput. Chem.* **18,** 1463–1472
44. Essmann, U., Perera, L., Berkowitz, M. L., Darden, T., Lee, H., and Pedersen, L. G. (1995) A smooth particle mesh Ewald potential. *J. Chem. Phys.* **103,** 8577– 8592
45. Humphrey, W., Dalke, A., and Schulten, K. (1996) VMD—Visual Molecular Dynamics. *J. Mol. Graph.* **14,** 33–38
46. Kazanietz, M. G., and Lemmon, M. A. (2011) Protein kinase C regulation: C1 meets C-tail. *Structure* **19,** 144 –146
47. Wu, W. I., Voegtli, W. C., Sturgis, H. L., Dizon, F. P., Vigers, G. P., and Brandhuber, B. J. (2010) Crystal structure of human AKT1 with an allosteric inhibitor reveals a new mode of kinase inhibition. *PLoS One* **5,** e12913
48. DiNitto, J. P., Delprato, A., Gabe Lee, M. T., Cronin, T. C., Huang, S., Guilherme, A., Czech, M. P., and Lambright, D. G. (2007) Structural basis and mechanism of autoregulation in 3-phosphoinositide-dependent Grp1 family Arf GTPase exchange factors. *Mol. Cell* **28,** 569 –583
49. Neumann, P., Weidner, A., Pech, A., Stubbs, M. T., and Tittmann, K. (2008) Structural basis for membrane binding and catalytic activation of the peripheral membrane enzyme pyruvate oxidase from *Escherichia coli*. *Proc. Natl. Acad. Sci. U.S.A.* **105,** 17390 –17395
50. Weidner, A., Neumann, P., Pech, A., Stubbs, M. T., and Tittmann, K. (2009) New insights into the membrane-binding and activation mechanism of pyruvate oxidase from *Escherichia coli, J. Mol. Catal. B Enzym.* **61,** 88 –92
51. Huse, M., and Kuriyan, J. (2002) The conformational plasticity of protein kinases. *Cell* **109,** 275–282
52. Filippakopoulos, P., Müller, S., and Knapp, S. (2009) SH2 domains: modulators of nonreceptor tyrosine kinase activity. *Curr. Opin. Struct. Biol.* **19,** 643– 649
53. Xu, W., Doshi, A., Lei, M., Eck, M. J., and Harrison, S. C. (1999) Crystal structures of c-Src reveal features of its autoinhibitory mechanism. *Mol. Cell* **3,** 629 – 638
54. Fuentes, E. J., Der, C. J., and Lee, A. L. (2004) Ligand-dependent dynamics and intramolecular signaling in a PDZ domain. *J. Mol. Biol.* **335,** 1105–1115
55. Pattridge, K. A., Weber, C. H., Friesen, J. A., Sanker, S., Kent, C., and Ludwig, M. L. (2003) Glycerol-3-phosphate cytidylyltransferase: structural changes induced by binding of CDP-glycerol and the role of lysine residues in catalysis. *J. Biol. Chem.* **278,** 51863–51871
56. Malabanan, M. M., Amyes, T. L., and Richard, J. P. (2010) A role for flexible loops in enzyme catalysis. *Curr. Opin. Struct. Biol.* **20,** 702–710
57. Desamero, R., Rozovsky, S., Zhadin, N., McDermott, A., and Callender, R. (2003) Active site loop motion in triosephosphate isomerase: T-jump relaxation spectroscopy of thermal activation. *Biochemistry* **42,** 2941–2951
58. Khajehpour, M., Wu, L., Liu, S., Zhadin, N., Zhang, Z.-Y., and Callender, R. (2007) Loop dynamics and ligand binding kinetics in the reaction catalyzed by the *Yersinia* protein tyrosine phosphatase. *Biochemistry* **46,** 4370 – 4378
59. Nashine, V. C., Hammes-Schiffer, S., and Benkovic, S. J. (2010) Coupled motions in enzyme catalysis. *Curr. Opin. Chem. Biol.* **14,** 644 – 651
60. Whittier, S. K., Hengge, A. C., and Loria, J. P. (2013) Conformational motions regulate phosphoryl transfer in related protein tyrosine phosphatases. *Science* **341,** 899 –903
61. Arsenault, D. J., Yoo, B. H., Rosen, K. V., and Ridgway, N. D. (2013) Ras-induced up-regulation of CTP:phosphocholine cytidylyltransferase α contributes to malignant transformation of intestinal epithelial cells. *J. Biol. Chem.* **288,** 633– 643
62. Gautier, R., Douguet, D., Antonny, B., and Drin, G. (2008) HELIQUEST: a web server to screen sequences with specific α-helical properties. *Bioinformatics* **24,** 2101–2102